

Electronic Supplementary Information

**Local Electric Field Favours More than Exposed Nitrogen Atoms on CO₂
Capture: a Case Study on the rht-type MOF Platform**

**Wen-Yang Gao,^a Tony Pham,^a Katherine A Forrest,^a Brian Space,^a Lukasz
Wojtas,^a Yu-Sheng Chen^b and Shengqian Ma^{*,a}**

^a *Department of Chemistry, University of South Florida, 4202 East Fowler Avenue,
Tampa, Florida, 33620, United States, Fax: +1 813-974-3203; Tel: +1 813-974-5217;
E-mail: sqma@usf.edu*

^b *ChemMatCARS, Center for Advanced Radiation Sources, The University of Chicago,
9700 S. Cass Avenue, Argonne, Illinois 60439, United States.*

Characterization

The powder X-ray diffraction (PXRD) data for **rht**-MOF-1 and **rht**-MOF-pyr were collected using a Bruker D8 Advance, $\text{CuK}\alpha$, $\lambda = 1.54178 \text{ \AA}$ (40 kV, 40 mA), at a range of 5 to 30° (2θ) and a stepsize of 0.5s/0.02° (2θ). The activated samples following adsorption tests were handled in the glovebox and loaded on the PXRD airtight specimen holder ring with dome to prevent moisture adsorption from air. Thermogravimetric analysis was performed on a TGA Q50 (TA-Instruments-Waters LLC.) in the range of 25-500 °C with a rate 10 °C/min. Gas adsorption isotherms of **rht**-MOF-1 and **rht**-MOF-pyr were collected using micromeritics surface area analyzer ASAP 2020. Before the measurements, the freshly prepared sample was repeatedly exchanged with methanol over 3 days. The sample was dried on the Schlenk line overnight at room temperature and then activated by using the “degas” function of ASAP 2020 for 6 hours at 85 °C. N_2 and H_2 adsorption isotherms were measured at 77 K using a liquid nitrogen bath. CO_2 and CH_4 adsorption isotherms were measured at 273 K using a water-ice bath and at 298K with a water bath.

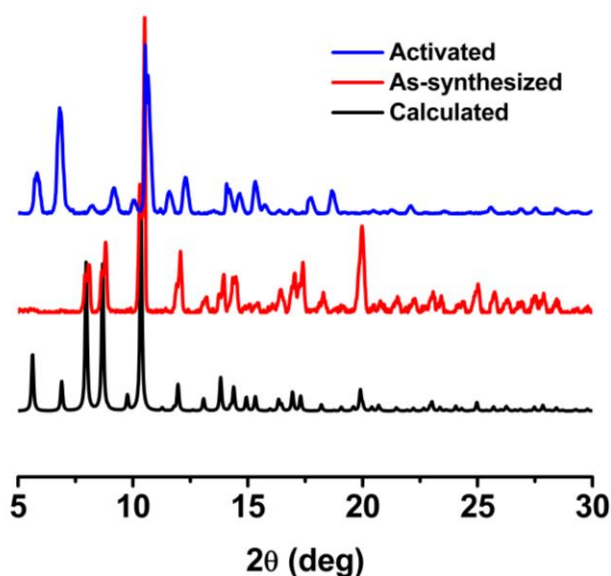


Fig. S1. Powder X-ray diffraction patterns of **rht**-MOF-1.

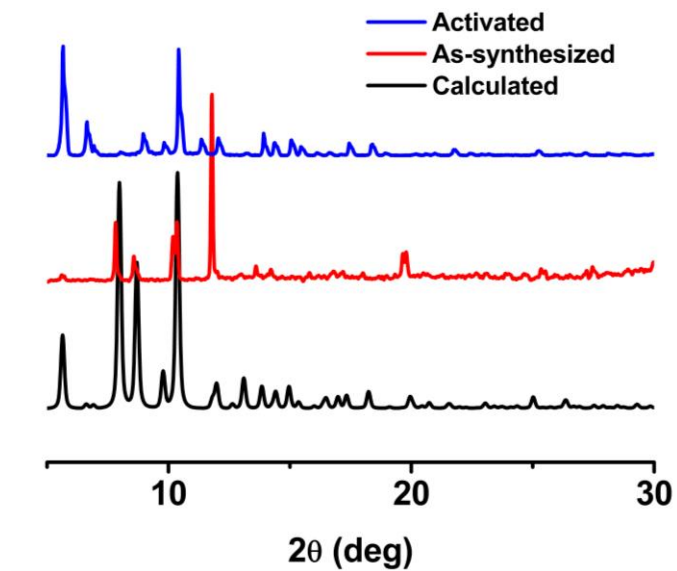


Fig. S2. Powder X-ray diffraction patterns of **rht-MOF-pyr**.

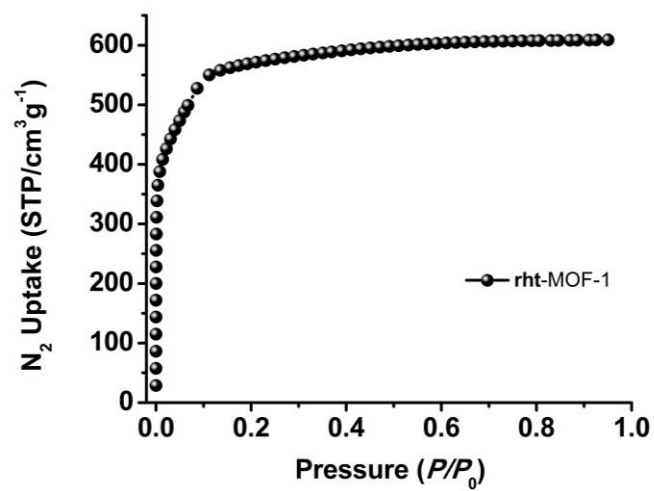


Fig. S3. N₂ adsorption isotherm of **rht-MOF-1** at 77 K.

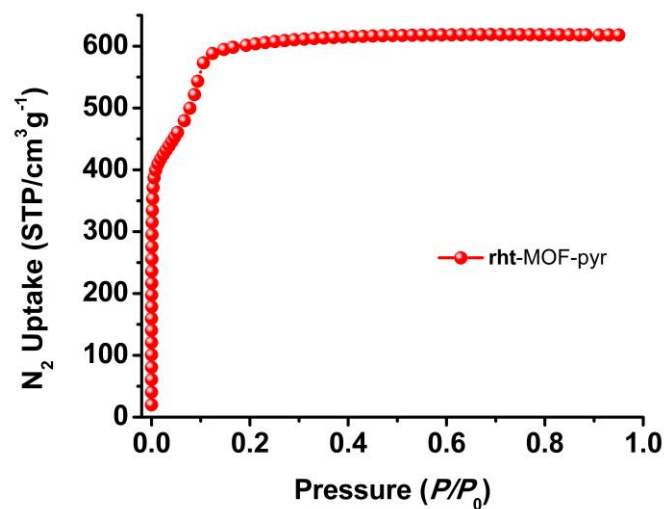


Fig. S4. N₂ adsorption isotherm of **rht-MOF-pyr** at 77 K.

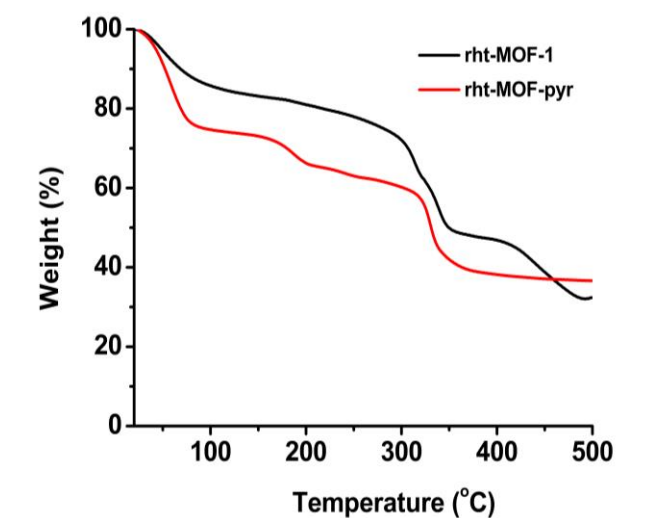


Fig. S5. Thermogravimetric analysis plots of activated **rht-MOF-1** and **rht-MOF-pyr**.

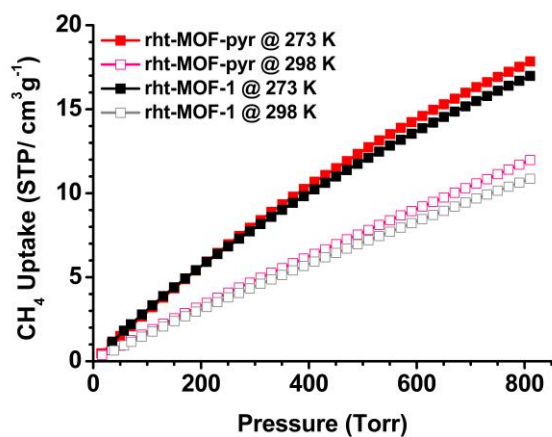


Fig. S6. CH₄ adsorption isotherms of **rht-MOF-1** and **rht-MOF-pyr** at 273 K and 298 K.

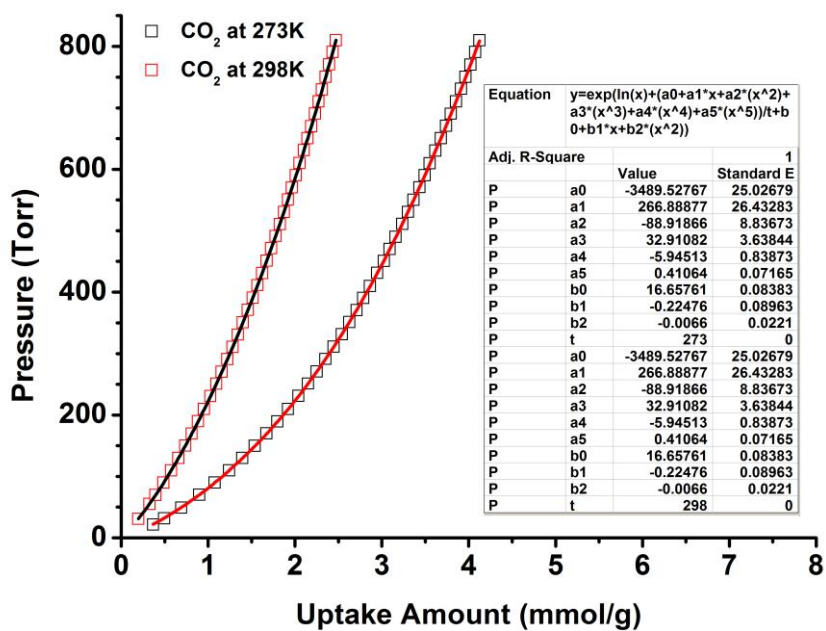


Fig. S7. Virial fitting of CO₂ adsorption isotherms of **rht-MOF-1** at 273K and 298K.

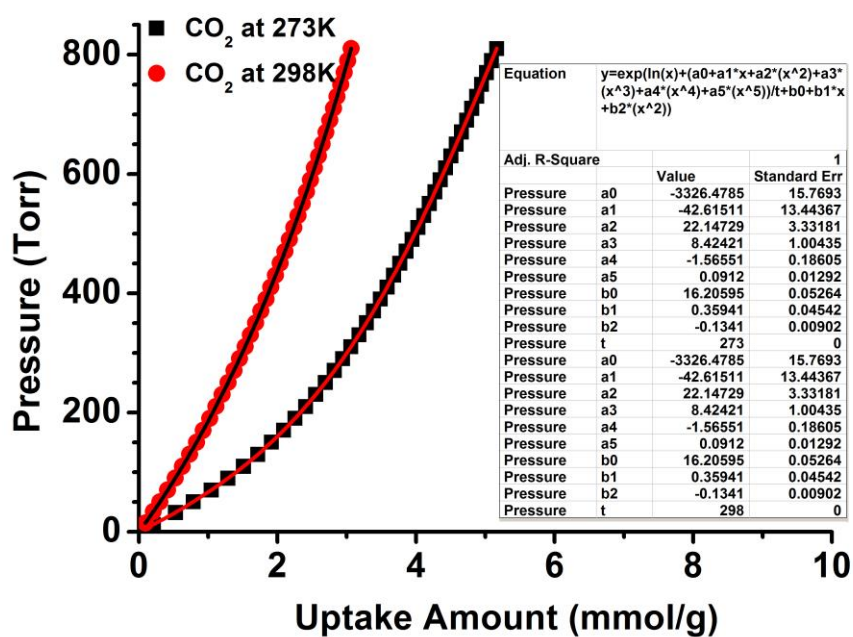


Fig. S8. Virial fitting of CO₂ adsorption isotherms of **rht-MOF-pyr** at 273 K and 298 K.

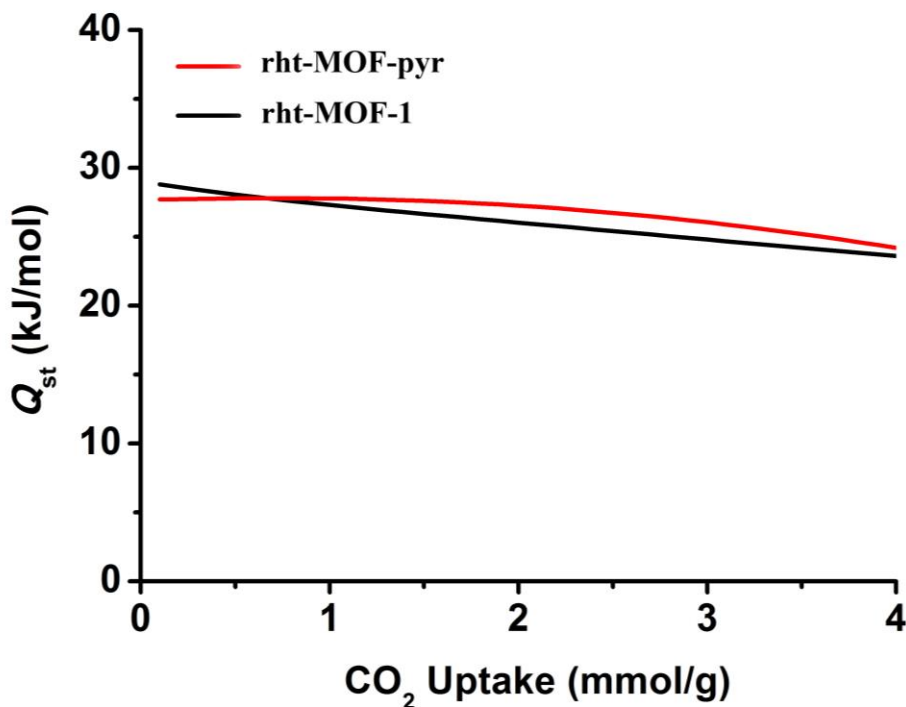


Fig. S9. CO₂ heats of adsorption of **rht-MOF-1** and **rht-MOF-pyr**.

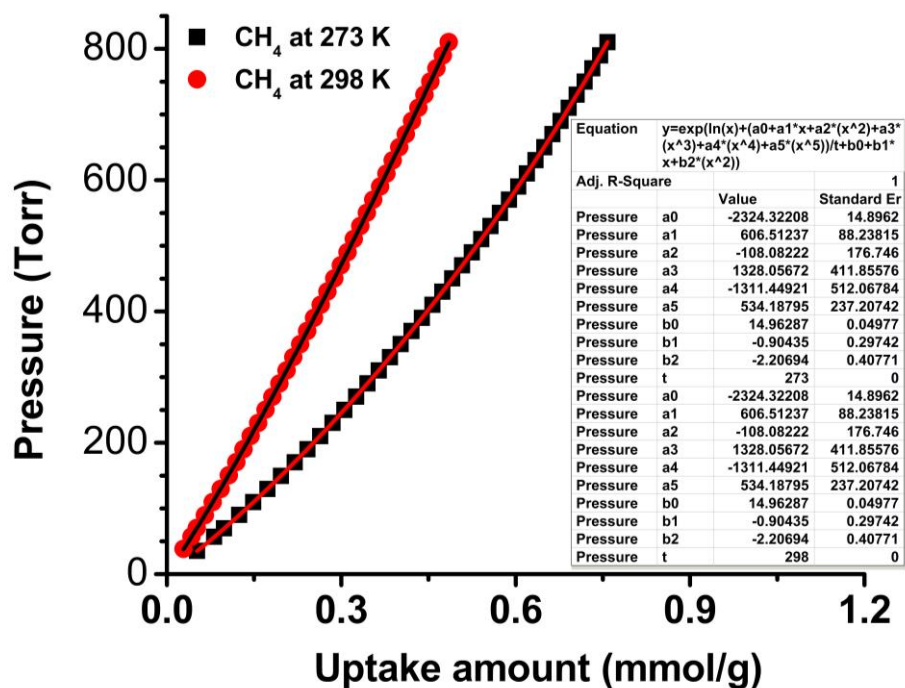


Fig. S10. Virial fitting of CH₄ adsorption isotherms of **rht**-MOF-1 at 273K and 298K.

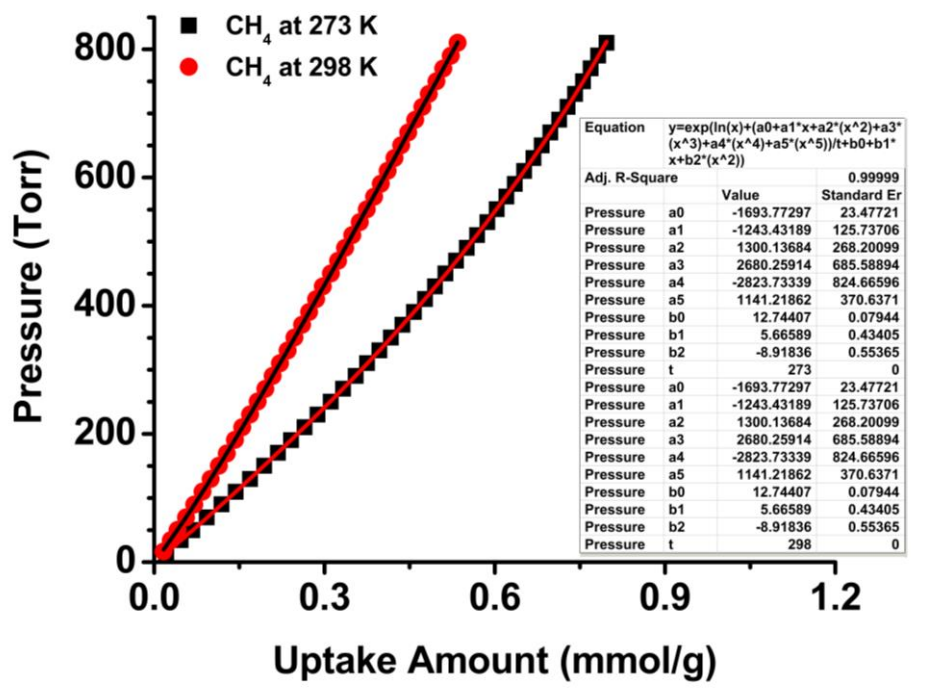


Fig. S11. Virial fitting of CH₄ adsorption isotherms of **rht**-MOF-pyr at 273K and 298K.

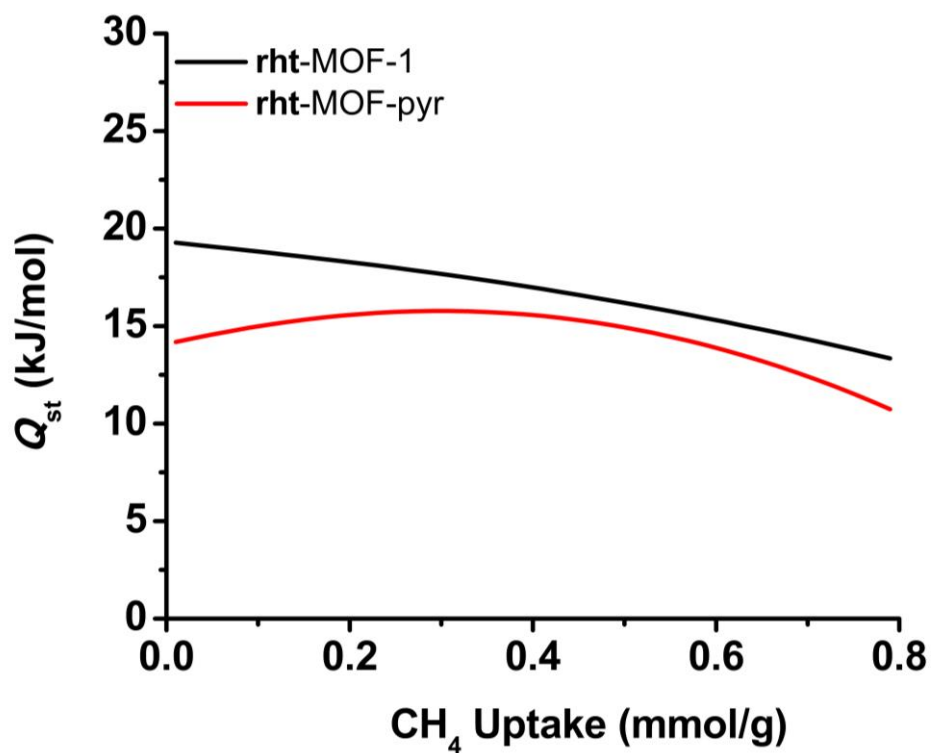


Fig. S12. CH₄ heats of adsorption of **rht-MOF-1** and **rht-MOF-pyr**.

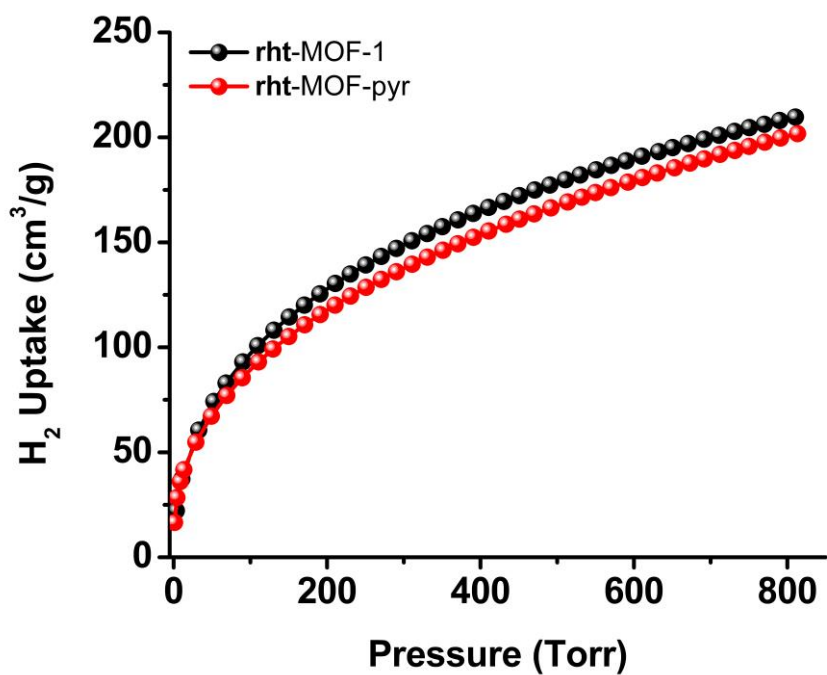


Fig. S13. H₂ adsorption isotherms of **rht-MOF-1** and **rht-MOF-pyr** at 77 K.

The virial equation of the form given in Equation (1) was employed to calculate the enthalpies of adsorption for CO₂ and CH₄.

$$\ln P = \ln N + 1/T \sum_{i=0}^m a_i N^i + \sum_{i=0}^n b_i N^i \quad (1)$$

where P is the pressure expressed in Torr, N is the amount adsorbed in mmol/g, T is the temperature in K, a_i and b_i are virial coefficients, and m and n represent the number of coefficients required to adequately describe the isotherms. The equation was fitted by using the the least-squares method; m and n were gradually increased until the contribution of a and b coefficients toward the overall fitting is statistically trivial, as determined by the t-test. The values of the virial coefficients $a_0 \dots a_m$ were then used to calculate the isosteric heat of adsorption by the following expression:

$$Q_{st} = -R \sum_{i=0}^m a_i N^i \quad (2)$$

Computational Studies

A. MOF Parametrization

All simulations were performed in a single unit cell of the respective **rht**-MOFs. Unless otherwise stated, the MOF–adsorbate interaction energy was represented by the sum of repulsion/dispersion, stationary electrostatics, and induced dipole energies. These were calculated using the Lennard-Jones potential, partial charges with Ewald summation,¹ and a Thole-Applequist type many-body polarization model,^{2–5} respectively. The Lennard-Jones parameters (ϵ and σ) for all atoms were taken from the Universal Force Field (UFF).⁶ The partial charges for the atoms in **rht**-MOF-1 and **rht**-MOF-pyr, as calculated using the Connolly charge-fitting scheme for both MOFs,⁷ were determined in previous work⁸ and used in this study. Many-body

polarization effects were parametrized using atomic point polarizabilities. The polarizabilities for all C, H, N, and O atoms were taken from van Duijnen et al.,⁹ while the polarizabilities for Cu²⁺ was determined in previous work¹⁰ and used herein. CO₂ was represented as a five-site explicit polarization model that was developed and used in previous work.¹¹ All simulations were performed using the Massively Parallel Monte Carlo (MPMC) code.¹²

All MOF atoms were constrained to be rigid for the simulations in this work. Further, the simulations were performed with all nitrate counterions positioned in the corners of the truncated tetrahedral cages in the respective **rht**-MOFs. This is the energy minimum position of the nitrate ions in these MOFs as determined in previous work on **rht**-MOF-1.^{8,13,14} It should be noted that this is the position for the nitrate ions in these **rht**-MOFs at low temperatures. At room temperature, MD simulations revealed that the nitrate ions are mobile in the MOFs and can migrate to other regions in the structure. Nevertheless, the simulations were performed at room temperature with the nitrate ions held fixed in the corners of the truncated tetrahedral cages. This approximation seemed appropriate since the interactions between the CO₂ molecules and the Cu₃O trimer units as well as the interactions between the CO₂ molecules and the [Cu₂(CO₂R)₄] clusters in each **rht**-MOF were the main interests in this work.

B. Canonical Monte Carlo Simulations

Canonical Monte Carlo (CMC) simulations of CO₂ adsorption were performed in **rht**-MOF-1 and **rht**-MOF-pyr to determine the favorable CO₂ adsorption sites in these MOFs. The simulations were performed in the canonical ensemble; in this method, the adsorbate particle number, the volume of the simulation box, and the temperature are held constant while other thermodynamic variables are allowed to fluctuate. Initially, 100 CO₂ molecules were simulated in each **rht**-MOF at 298 K. The simulations continued until equilibrium was reached (approximately 1×10^6 MC steps). Afterwards, the regions of high CO₂ occupancy in each MOF were identified.

For both **rht**-MOFs, the favored CO₂ adsorption sites were the nitrate ions, the metal paddlewheels, and the Cu₃O trimers.

Since it was hypothesized that the main difference in the CO₂ adsorption capacities between the **rht**-MOFs was attributed to the interaction between the CO₂ molecules and the Cu₃O trimers, additional calculations about the Cu₃O trimers were considered. Thus, the energetic minima for a single CO₂ molecule about the Cu₃O trimers in both **rht**-MOFs were determined using simulated annealing.¹⁵ This method involves simulating at an initial temperature and scaling down periodically over the course of the simulation, causing the sorbate molecule to settle into the most energetically favorable position as the system cools. In this work, an initial temperature of 298 K was selected, and this temperature was scaled by 0.9999 after every 1000 simulation steps. The simulation continued until the temperature dropped below 20 K. Subsequently, the most favorable orientation of the CO₂ molecule about the Cu₃O trimers in each **rht**-MOF was identified.

C. Grand Canonical Monte Carlo Simulations

1. Simulated Adsorption Isotherms

Grand canonical Monte Carlo (GCMC) simulations of CO₂ adsorption were performed in **rht**-MOF-1 and **rht**-MOF-pyr to predict the adsorption isotherms in both MOFs. The simulations were performed in the grand canonical ensemble, in which the chemical potential, volume, and temperature of the simulation box are held constant while other thermodynamic variables (e.g., adsorbate particle number) are allowed to fluctuate.¹⁶ The simulations were performed at 298 K for pressures ranging from 0 to 1 atm in both MOFs. For each state point considered, the simulations initially consisted of 1×10^6 MC steps to guarantee equilibration. Afterward, the simulations continued for an additional 1×10^6 MC steps to sample the desired thermodynamic properties and to ensure reasonable averages for the adsorbate particle number. Fig. S14 shows the simulated CO₂ adsorption isotherms for both MOFs at

298 K and pressures up to 1 atm. Consistent with experimental measurements, the simulations showed that the CO₂ uptake is higher for **rht**-MOF-pyr than **rht**-MOF-1 for all pressures considered.

In this work, additional simulations of CO₂ adsorption were performed in both **rht**-MOFs where only the repulsion/dispersion potential energy was calculated. For simulations at 298 K and pressures up to 760 Torr, the simulations still revealed that **rht**-MOF-pyr adsorbs more CO₂ than **rht**-MOF-1 even though electrostatic and induction interactions are not taken into account (Fig. S15). This could be due to the fact that the C–H groups of the pyrazolate moieties in **rht**-MOF-pyr provides for more favorable van der Waals interactions towards the CO₂ molecules than the carbon-coordinated N atoms of the tetrazolate moieties in **rht**-MOF-1.

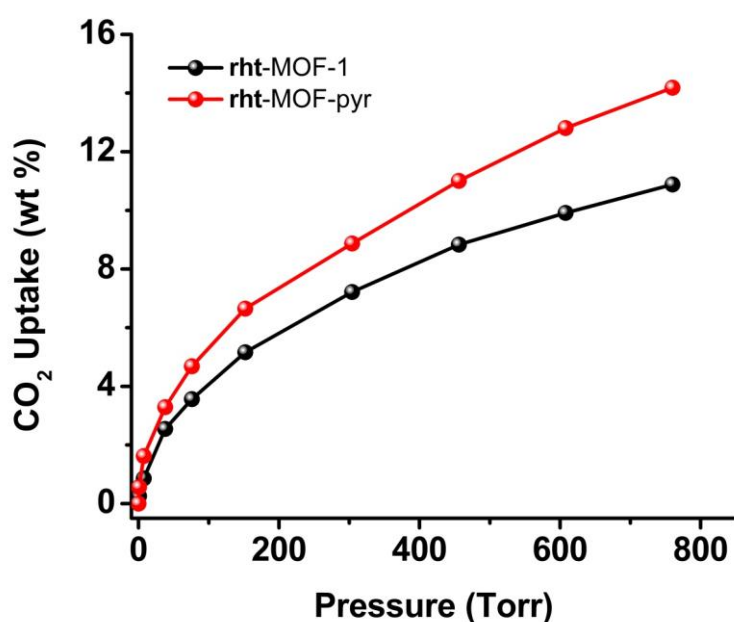


Fig. S14. Simulated CO₂ adsorption isotherms for **rht**-MOF-1 and **rht**-MOF-pyr at 298 K and pressures up to 760 Torr.

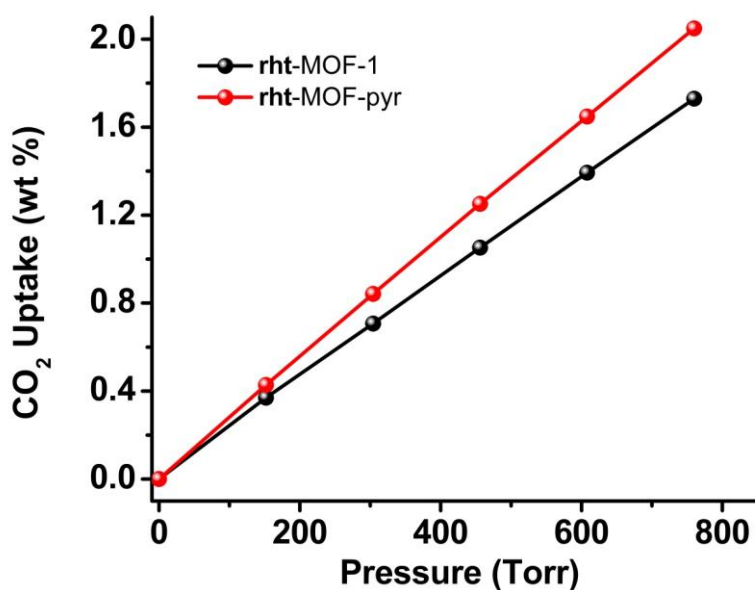


Fig. S15. Simulated CO₂ adsorption isotherms for **rht**-MOF-1 and **rht**-MOF-pyr at 298 K and pressures up to 760 Torr, where only the repulsion/dispersion interaction energy was calculated.

2. Radial Distribution Functions

In **rht**-MOF-1 and **rht**-MOF-pyr, there are three chemically distinct Cu²⁺ ions in the crystal structures of these MOFs (Fig. S16).^{8,14} The Cu1 ions are part of the copper paddlewheels and face towards the center of the ligand. The Cu2 ions are also part of the paddlewheel, but face away from the center of the ligand. In the **rht**-MOF environment, the Cu1 ions project into the truncated tetrahedral (T-*T_d*) and truncated octahedral cages (T-*O_h*), while the Cu2 ions project into the cuboctahedral cages (cub-*O_h*). The Cu3 ions are those Cu²⁺ ions that are part of the Cu₃O trimers.

The radial distribution functions, $g(r)$, of adsorbed CO₂ molecules about all three types of Cu²⁺ ions in **rht**-MOF-1 and **rht**-MOF-pyr at 298 K and pressures of 0.01 and 1 atm (7.60 Torr and 760 Torr), as generated from GCMC simulation, are shown

in Fig. S17. At 0.01 atm (7.60 Torr), a large nearest-neighbor peak can be observed around the Cu1 ions in **rht**-MOF-1 and the Cu2 ions in **rht**-MOF-pyr at a distance of approximately 3.3 Å. This signifies that there are a large number of CO₂ molecules adsorbing onto those Cu²⁺ ions in the respective MOFs at low pressure, with an interaction distance of about 3.3 Å between the Cu²⁺ ion and the carbon atom of the CO₂ molecule. This distance is comparable to the corresponding distance that has been observed in the MOF HKUST-1 through neutron powder diffraction studies (3.0 to 3.2 Å).¹⁷ These peaks observed in the $g(r)$ around the Cu1 ions in **rht**-MOF-1 and the Cu2 ions in **rht**-MOF-pyr are notably reduced in magnitude at 1 atm (760 Torr). This is because there is lesser relative population of CO₂ molecules adsorbing onto these Cu²⁺ ions in the respective MOFs at higher pressures.

Fig. S17 shows that there is a small population of CO₂ molecules adsorbing onto the Cu2 ions in **rht**-MOF-1 and the Cu1 ions in **rht**-MOF-pyr at both pressures, with occupancy becoming slightly more noticeable at the higher pressure. This is because these Cu²⁺ ions are not as favored in the respective **rht**-MOFs. Indeed, the simulations revealed that the CO₂ molecules prefer to adsorb onto the Cu1 ions in **rht**-MOF-1 and the Cu2 ions in **rht**-MOF-pyr. The reason for this is because, as determined through electronic structure calculations, the Cu1 ions have a significantly higher partial positive charge than the Cu2 ions in **rht**-MOF-1, whereas the effect is reversed in the case of **rht**-MOF-pyr.⁸ The adsorbate molecules will bind initially onto the type of Cu²⁺ ion that exhibits the greater partial positive charge.

Fig. S17 also shows that the peak that represents the adsorption of CO₂ molecules onto the Cu3 ions in **rht**-MOF-1 and **rht**-MOF-pyr is higher in magnitude at 1 atm (760 Torr). Indeed, at 0.01 atm (7.60 Torr), there is a small population of CO₂ molecules adsorbing onto these Cu3 ions compared to at 1 atm (760 Torr) in both MOFs. The fact that the nearest-neighbor peak observed in the $g(r)$ around the Cu3 ions is larger at 1 atm (760 Torr) than at 0.01 atm (7.60 Torr) in both MOFs implies that the Cu3 ions are becoming occupied at higher loadings. The $g(r)$ of adsorbed CO₂

molecules about the Cu₃ ions at 298 K and pressures of 0.01 and 1 atm (7.60 and 760 Torr) are plotted together for both **rht**-MOFs in Fig. S18. This direct comparison of the $g(r)$ around the Cu₃ ions show that there are more CO₂ molecules adsorbing onto these ions in **rht**-MOF-pyr compared to **rht**-MOF-1 at both pressures considered. This confirms the notion that Cu²⁺ ions that are part of the Cu₃O trimers are more favorable for CO₂ adsorption in **rht**-MOF-pyr than **rht**-MOF-1.

Overall, two main conclusions can be reached from analyzing the $g(r)$ results: (1) the Cu1 ions are the preferred metal binding sites in **rht**-MOF-1 at low loading, whereas the Cu2 ions are the favorable metal binding sites in **rht**-MOF-pyr under similar conditions; (2) the Cu3 ions become more occupied at higher loadings in both MOFs, with more CO₂ molecules adsorbing onto these ions in **rht**-MOF-pyr.

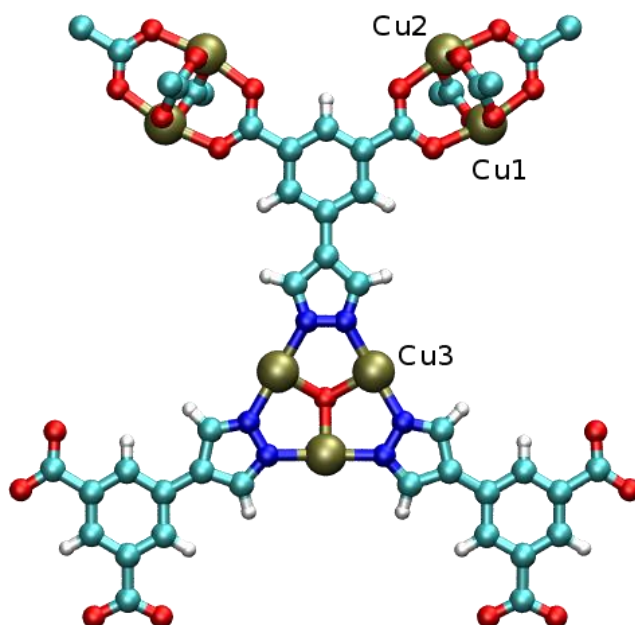
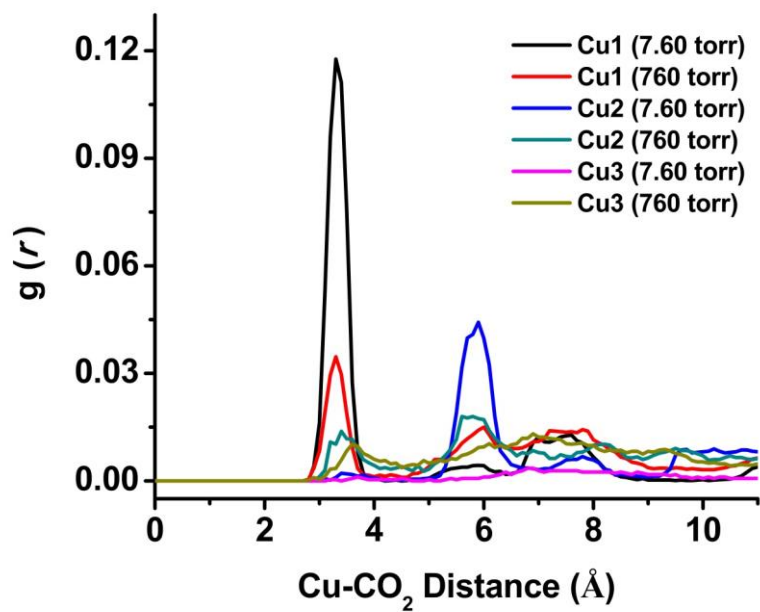
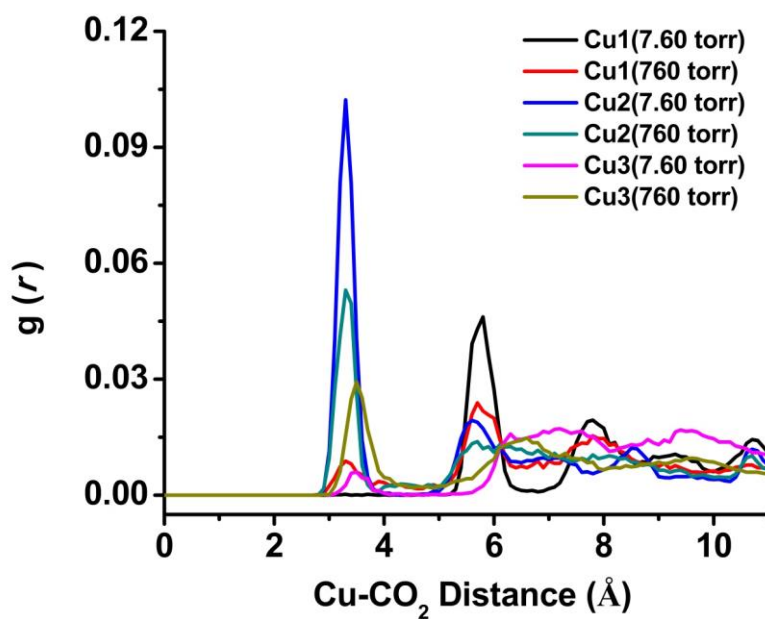


Fig. S16. The ligand, copper paddlewheel, and Cu₃O trimer units in **rht**-MOF-pyr showing the labeling of the Cu1, Cu2, and Cu3 ions. A similar label for the different Cu²⁺ ions can be used for **rht**-MOF-1. Atom colors: C = cyan, H = white, N = blue, O = red, Cu = gold.



(a)



(b)

Fig. S17. Radial distribution functions, $g(r)$, about the Cu1 ions, Cu2 ions, and Cu3 ions in (a) **rht**-MOF-1 and (b) **rht**-MOF-pyr at 298 K and pressures of 0.01 atm (7.60 Torr) and 1 atm (760 Torr).

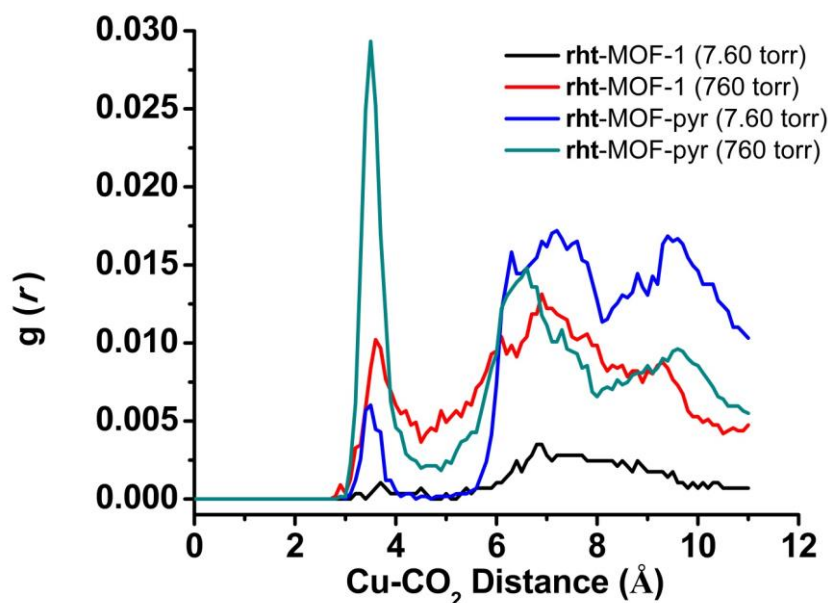


Fig. S18. Radial distribution functions, $g(r)$, about Cu3 ions in **rht**-MOF-1 and **rht**-MOF-pyr at 298 K and pressures of 0.01 atm (7.60 Torr) and 1 atm (760 Torr).

D. Density Functional Theory Calculations

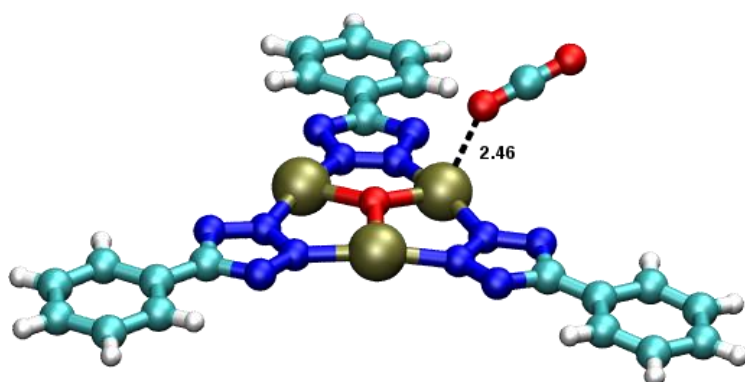
In this study, density functional theory (DFT) calculations were performed for a single CO₂ molecule positioned about the [Cu₃O(N_{4-x}(CH)_xCR)₃] ($x = 0$ or 2) unit for both **rht**-MOFs. This was done to investigate the significance of substituting tetrazolate with pyrazolate on CO₂ adsorption and to assess the difference in the MOF-CO₂ interaction strength through quantum mechanical calculations. The reduced hexatopic building unit (RHBU), where all carboxylate groups of the hexatopic building unit are replaced with optimized H atoms, from both MOFs was

considered for the calculations. First, a CO₂ molecule was placed in proximity to a Cu²⁺ ion of the Cu₃O trimer unit in both RHBUs. The CO₂ molecule was then optimized to an energetically favorable position within both RHBUs using the NWChem *ab initio* software¹⁸ and with the well-known B3LYP functional.¹⁹ For this calculation, the 6-31G* basis set was used for all C, H, N, and O atoms, whereas the LANL2DZ effective core potential basis set²⁰ was used for Cu²⁺ since a large basis set was required to treat the inner electrons of this many-electron species. The optimized positions of the CO₂ molecule within the RHBUs for **rht**-MOF-1 and **rht**-MOF-pyr are displayed in Fig. S19. The optimization calculations revealed that the CO₂ molecule is positioned in line with the pyrazolate groups in **rht**-MOF-pyr, where the O atom of the CO₂ molecule interacts with the Cu²⁺ ion and the H atoms of the pyrazolate groups concurrently. In contrast, the CO₂ molecule prefers to be oriented at an angle with respect to the [Cu₃O(N₄CR)₃] trimer to minimize O–N interactions between the CO₂ molecule and the tetrazolate groups in **rht**-MOF-1.

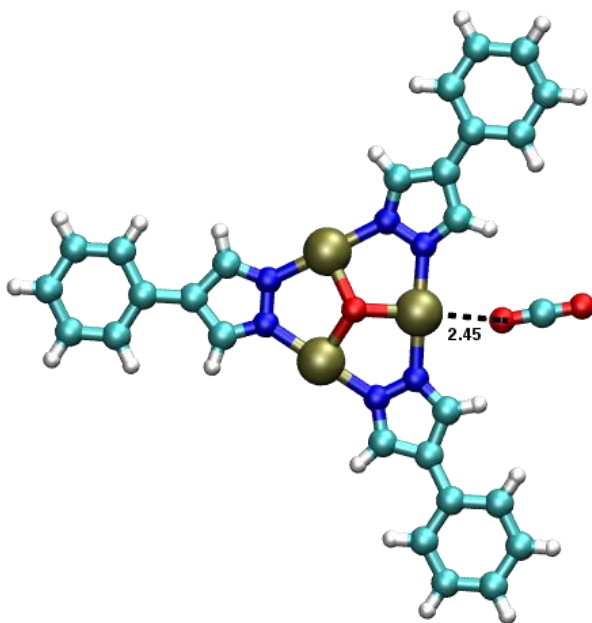
Calculation of the binding energy for the CO₂ molecule positioned about the Cu₃O trimer in both RHBUs was also performed using DFT. As with the optimizations, the binding energy calculations were also computed using the NWChem software. The same functional and basis sets for all atoms as described above were used for the calculations. The binding energy for the RHBUs–CO₂ interaction was calculated *via* the following:

$$\Delta E = E(A + B) - [E(A) + E(B)]$$

where A represents the RHBUs and B represents the CO₂ molecule. The calculations revealed that the binding energy for the RHBUs–CO₂ interaction for **rht**-MOF-1 and **rht**-MOF-pyr are -21.3 and -22.6 kJ mol⁻¹, respectively.



(a)



(b)

Fig. S19. The optimized position of a CO₂ molecule about the Cu₃O trimer within the reduced hexatopic building unit in (a) **rht**-MOF-1 and (b) **rht**-MOF-pyr as determined using density functional theory (DFT). The distances (Å) between the Cu²⁺ ion and the closest O atom of the CO₂ molecule are also shown. Atom colors: C = gray, H = white, N= blue, O = red, Cu = gold.

References

- 1.) Ewald, P. P.; *Ann. Phys.* **1921**, 369, 253–287.
- 2.) Applequist, J.; Carl, J. R.; Fung, K.-K. *J. Am. Chem. Soc.* **1972**, 94, 2952–2960.
- 3.) Thole, B. *Chem. Phys.* **1981**, 59, 341–350.
- 4.) Bode, K. A.; Applequist, J. *J. Phys. Chem.* **1996**, 100, 17820–17824.
- 5.) McLaughlin, K.; Cioce, C. R.; Pham, T.; Belof, J. L.; Space, B. *J. Chem. Phys.* **2013**, 139, 184112.
- 6.) Rappé, A. K.; Casewit, C. J.; Colwell, K. S.; Goddard, W. A.; Skiff, W. M. *J. Am. Chem. Soc.* **1992**, 114, 10024–10035.
- 7.) Singh, U. C.; Kollman, P. A. *J. Comput. Chem.* **1984**, 5, 129–145.
- 8.) Gao, W.-Y.; Cai, R.; Pham, T.; Forrest, K. A.; Hogan, A.; Nugent, P.; Williams, K.; Wojtas, L.; Luebke, R.; Weselinski, L. J.; Zaworotko, M. J.; Space, B.; Chen, Y.-S.; Eddaoudi, M.; Shi, X.; Ma, S. *Chem. Mater.* **2015**, 27, 2144–2151.
- 9.) van Duijnen, P. T.; Swart, M. *J. Phys. Chem. A* **1998**, 102, 2399–2407.
- 10.) Forrest, K. A.; Pham, T.; McLaughlin, K.; Belof, J. L.; Stern, A. C.; Zaworotko, M. J.; Space, B. *J. Phys. Chem. C* **2012**, 116, 15538–15549.

- 11.) Mullen, A. L.; Pham, T.; Forrest, K. A.; Cioce, C. R.; McLaughlin, K.; Space, B. *J. Chem. Theory Comput.* **2013**, *9*, 5421–5429.
- 12.) Belof, J. L.; Space, B. Massively Parallel Monte Carlo (MPMC). 2012. Available on GitHub. <https://github.com/mpmccode/mpmc>.
- 13.) Babarao, R.; Eddaoudi, M.; Jiang, J. W. *Langmuir* **2010**, *26*, 11196–11203.
- 14.) Pham, T.; Forrest, K. A.; Hogan, A.; McLaughlin, K.; Belof, J. L.; Eckert, J.; Space, B. *J. Mater. Chem A* **2014**, *2*, 2088–2100.
- 15.) Kirkpatrick, S.; Gelatt, C. D.; Vecchi, M. P. *Science* **1983**, *220*, 671–680.
- 16.) Metropolis, N.; Rosenbluth, A. W.; Rosenbluth, M. N.; Teller, A. H.; Teller, E. *J. Chem. Phys.* **1953**, *21*, 1087–1092.
- 17.) Wu, H.; Simmons, J. M.; Srinivas, G.; Zhou, W.; Yildirim, T. *J. Phys. Chem. Lett.* **2010**, *1*, 1946–1951.
- 18.) Valiev, M.; Bylaska, E.; Govind, N.; Kowalski, K.; Straatsma, T.; Dam, H. V.; Wang, D.; Nieplocha, J.; Apra, E.; Windus, T.; de Jong, W. *Comput. Phys. Commun.* **2010**, *181*, 1477–1489.
- 19.) (a) Becke, A. D. *J. Chem. Phys.* **1993**, *98*, 5648–5652. (b) Lee, C.; Yang, W.; Parr, R. G. *Phys. Rev. B* **1988**, *37*, 785–789. (c) Vosko, S. H.; Wilk, L.; Nusair, M. *Can. J. Phys.* **1980**, *58*, 1200–1211. (d) Stephens, P. J.; Devlin, F. J.; Chabalowski, C. F.; Frisch, M. J. *J. Phys. Chem.* **1994**, *98*, 11623–11627.
- 20.) (a) Stevens, W. J.; Basch, H.; Krauss, M. *J. Chem. Phys.* **1984**, *81*, 6026–6033. (b) Hay, P. J.; Wadt, W. R. *J. Chem. Phys.* **1985**, *82*, 270–283. (c) LaJohn, L. A.; Christiansen, P. A.; Ross, R. B.; Atashroo, T.; Ermler, W. C. *J. Chem. Phys.* **1987**, *87*, 2812–2824.